Controlling Superstructure-Property Relationships via Critical Casimir Assembly of Quantum Dots

Marino, Emanuele; Balazs, Daniel M.; Crisp, Ryan W.; Hermida-Merino, Daniel; Loi, Maria A.; Kodger, Thomas E.; Schall, Peter

DOI
10.1021/acs.jpcc.9b02033

Publication date
2019

Document Version
Final published version

Published in
Journal of Physical Chemistry C

Citation (APA)
Marino, E., Balazs, D. M., Crisp, R. W., Hermida-Merino, D., Loi, M. A., Kodger, T. E., & Schall, P. (2019). Controlling Superstructure-Property Relationships via Critical Casimir Assembly of Quantum Dots. *Journal of Physical Chemistry C*, *123*(22), 13451-13457. https://doi.org/10.1021/acs.jpcc.9b02033

THE JOURNAL OF PHYSICAL CHEMISTRY C

Article

Cite This: J. Phys. Chem. C 2019, 123, 13451−13457

pubs.acs.org/JPCC

Controlling Superstructure−Property Relationships via Critical Casimir Assembly of Quantum Dots

Emanuele Marino,[†,#] Daniel M. Balazs,[‡,▽] Ryan W. Crisp,[§] Daniel Hermida-Merino,[∥] Maria A. Loi,[‡] Thomas E. Kodger,[†,⊥] and Peter Schall*[,†]

[†]Van der Waals—Zeeman Institute, University of Amsterdam, Science Park 904, 1098 XH Amsterdam, The Netherlands

[‡]Zernike Institute for Advanced Materials, University of Groningen, Nijenborgh 4, 9747 AG Groningen, The Netherlands

[§]Chemical Engineering, Optoelectronic Materials, Delft University of Technology, Van der Maasweg 9, 2629 HZ Delft, The Netherlands

[∥]ESRF, 6 Rue Jules Horowitz, BP 220, F-38043 Grenoble Cedex 09, France

[⊥]Physical Chemistry and Soft Matter, Wageningen University & Research, Stippeneng 4, 6708 WE Wageningen, The Netherlands

Supporting Information

ABSTRACT: The assembly of colloidal quantum dots (QDs) into dense superstructures holds great promise for the development of novel optoelectronic devices. Several assembly techniques have been explored; however, achieving direct and precise control over the interparticle potential that controls the assembly has proven to be challenging. Here, we exploit the application of critical Casimir forces to drive the growth of QDs into superstructures. We show that the exquisite temperature-dependence of the critical Casimir potential offers new opportunities to control the assembly process and morphology of the resulting QD superstructures. The direct assembly control allows us to elucidate the relation between structural, optical, and conductive properties of the critical Casimir-grown QD superstructures. We find that the choice of the temperature setting the interparticle potential plays a central role in maximizing charge percolation across QD thin-films. These results open up new directions for controlling the assembly of nanostructures and their optoelectronic properties.

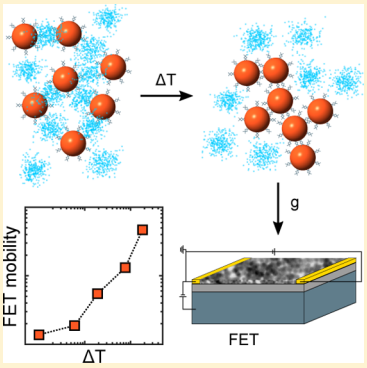

INTRODUCTION

At the nanoscale, quantum dots (QDs) act as building blocks in the development of a wide range of optoelectronic devices converting light into electric current, e.g., photodetectors and solar cells, or vice versa, LEDs and lasers.[1−3] For a device to operate, current must flow through the QD active film, provided the existence of percolative conductive paths.[4] The threshold for percolation depends on how efficiently the QD superstructure spans space and specifically on the number of conductive bonds a QD establishes with its neighbors.[5] These bonds are enabled by interdot quantum mechanical coupling[6] and can be epitaxial in nature,[7] mediated by inorganic molecular complexes[8] or conjugated ligands.[9] Maximizing the number of bonds in QD superstructures represents a modern grand challenge that must be addressed by controlling the assembly of QDs into superstructures.[10] However, commonly used fabrication techniques, such as spin coating, employ fast solvent evaporation thus offering little control over the structure of QD films. The resulting amorphous films permit conduction but preclude faster charge transport mechanisms requiring long-range order.[11] The short time scales imposed by spin coating do not allow for control of the QD pair potential, therefore limiting the fundamental understanding of QD interactions and device optimization.

Such interaction control has been well established in colloidal science, where the particle pair potential has been tailored by depletion,[12] magnetic,[13] or DNA-mediated interactions.[14] However, the long length scales of these interactions make them typically incompatible with the assembly of nanometer-sized QDs. Moreover, most interactions do not offer the possibility of continuously tuning their magnitude without irreversibly altering the composition of the dispersion. Recently, the critical Casimir effect has emerged as a novel temperature-tunable interaction to drive the assembly of colloidal particles mediated by the solvent alone.[15−18] The interaction has been measured[19] and modeled[20] for micrometer-sized colloidal particles. The tunability of this interaction resides on the exquisite role of temperature setting the length scale of solvent fluctuations, enabling direct control over both the magnitude and length scale of the interparticle attraction down to the molecular scale.[19] This solvent-mediated interaction offers new opportunities to drive the assembly of nanometer-sized QDs in solution.[21]

Here, we show that critical Casimir forces provide new control over the assembly of QD films. We use the

Received: March 3, 2019
Revised: April 26, 2019
Published: May 8, 2019

DOI: 10.1021/acs.jpcc.9b02033
J. Phys. Chem. C 2019, 123, 13451−13457

temperature-dependent solvent fluctuations to tune the QD interactions, to control QD film morphology, and to study the influence of morphology on film conductivity. The advantage of the critical Casimir force is that the length scale of solvent fluctuations is most compatible with the small size of the QDs, enabling their interaction control over a wide range of temperatures. Subjected to critical Casimir forces, the charge-stabilized QDs assemble into superstructures and subsequently deposit onto substrates. We study the properties of the resulting QD superstructures by optical spectroscopy and conductivity techniques. We find that while short-range conductivity between QDs is unaffected by morphological changes, the macroscopic conductivity increases by 2 orders of magnitude for lower attraction, thus suggesting that weaker attractive potentials maximize the number of long-range percolative pathways in the plane of conduction. We rationalize these findings with a pair potential model superimposing critical Casimir interactions onto standard van der Waals attraction and electrostatic repulsion, leading to temperature-dependent aggregation of both reversible and irreversible nature.

Hydrophobic CdSe QDs with diameter σ_{QD} = 6.5 nm are synthesized according to reported procedures and dispersed in hexane.[22,23] The native oleate ligands passivating the QD surface are then exchanged with short thiostannate complexes $(NH_4)_4Sn_2S_6$, making the QDs hydrophilic and allowing dispersion in the critical Casimir solvent.[8,24,25] The critical Casimir effect relies on the use of a mixture of two solvents, here water and 2,6-lutidine (Lut). Given a concentration of lutidine in water, c_{Lut}, the solvent mixture mixes homogeneously for temperatures $T < T_s$, and phase-separates into water-rich and Lut-rich phases for $T > T_s$, where T_s is the phase separation temperature (Figure 1a). Below and in proximity of the critical point of the dispersion, defined by the critical lutidine volume fraction $c_{Lut} = c_c$ = 30.2 v/v % and the critical temperature T_c = 307 K, solvent density fluctuations arise. These fluctuations can be described as spontaneous compositional variations resulting in locally water-rich or Lut-rich regions of average size ξ, the solvent correlation length. The confinement of solvent composition fluctuations between two walls or particle surfaces results in a net attractive force, known as the critical Casimir force.[26] The magnitude and length scale of this attraction strongly depend on the solvent correlation length, controlled by the distance $\Delta T = T_c - T$ from the critical temperature T_c according to $\xi(\Delta T) \sim \xi_0 \times (\Delta T/T_c)^{-0.63}$ at the critical composition.[27] The magnitude of the critical Casimir force can also be controlled by the solvent composition; choosing $\Delta c = c_{Lut} - c_c < 0$ will result in Lut-rich fluctuations, whereas $\Delta c > 0$ will result in water-rich fluctuations. The largest forces arise in solvents poor in the component preferred by the particles. Indeed, we have shown previously that hydrophilic QDs assemble in lutidine-rich solvents[21] due to the increased particle-fluctuation affinity;[28] therefore, we focus on lutidine-rich solvents here, choosing c_{Lut} = 32 v/v % > c_c.

METHODS

Chemicals. 2,6-Lutidine (redistilled, ≥99%) was purchased from Sigma-Aldrich and redistilled prior to use. Milli-Q water was used for all experiments. Hexanes (Sigma-Aldrich, ≥99%), acetonitrile (Sigma-Aldrich, ≥99.5%), and *N*-methylformamide (TCI, >99%) were used as received.

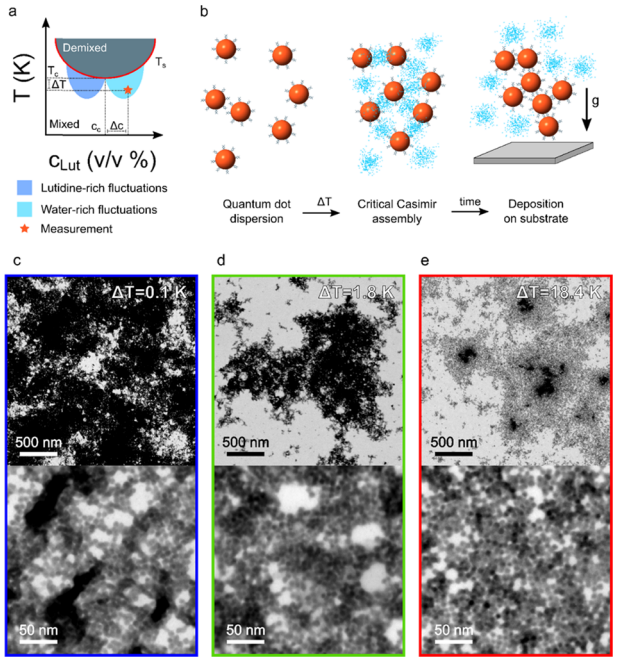

Figure 1. Quantum dot assembly by critical Casimir forces. (a) Schematic phase diagram of a binary mixture of water and 2,6-lutidine. Gray-shaded area indicates the demixed solvent, and the red boundary line indicates the solvent phase separation temperature, T_s. The colored-shaded areas below indicate regions in which lutidine-rich (dark blue) or water-rich (light blue) solvent density fluctuations arise. The critical temperature, T_c, and composition, c_c, are also indicated. (b) Schematic of the QD assembly by critical Casimir forces: dispersion of ligand-stabilized QDs (left), solvent density fluctuations (blue) arising upon decreasing ΔT, driving the assembly upon confinement by the QDs' surfaces (center), and assembled superstructures sedimenting onto the substrate (right). (c–e) Bright-field scanning transmission electron microscopy micrographs of QD superstructures assembled by critical Casimir forces, deposited on a transmission electron microscopy (TEM) grid for the measurement. Assembly time: 84 h.

QD Synthesis. QDs were synthesized according to published procedures.[22,23] QD concentration was established by using a published sizing curve.[29]

Ligand Synthesis and Exchange. The thiostannate complex $(NH_4)_4Sn_2S_6$ was synthesized as a 100 mM solution in water by following a published procedure.[24] The ligand exchange was performed by placing a 40 μM QD dispersion in hexanes (apolar phase) in contact with a 40 mM solution of $(NH_4)_4Sn_2S_6$ in *N*-methylformamide (polar phase) in a 1:1 volume ratio. The phase-separated system was stirred vigorously until the apolar phase became colorless (30 min). The apolar phase was then removed, and the polar phase was washed with clean hexanes; this procedure was repeated three times. The QDs were precipitated by adding acetonitrile in a 1:1 volume ratio with the polar phase and centrifuging at 3000*g* for 15 min. After removing the clear supernatant, QDs were fully redispersed in a binary mixture of water and lutidine (c_{Lut} = 32 v/v %) at a concentration of 40 μM.

Critical Casimir Assembly of QDs. The phase separation temperature T_s was determined prior to assembly by submerging a flame-sealed glass capillary containing the QD dispersion in the binary mixture in a thermostated water bath with a temperature stability of 0.01 K (Lauda ET15S). The temperature was increased at a rate of 0.01 K min^{-1} until

DOI: 10.1021/acs.jpcc.9b02033
J. Phys. Chem. C 2019, 123, 13451−13457

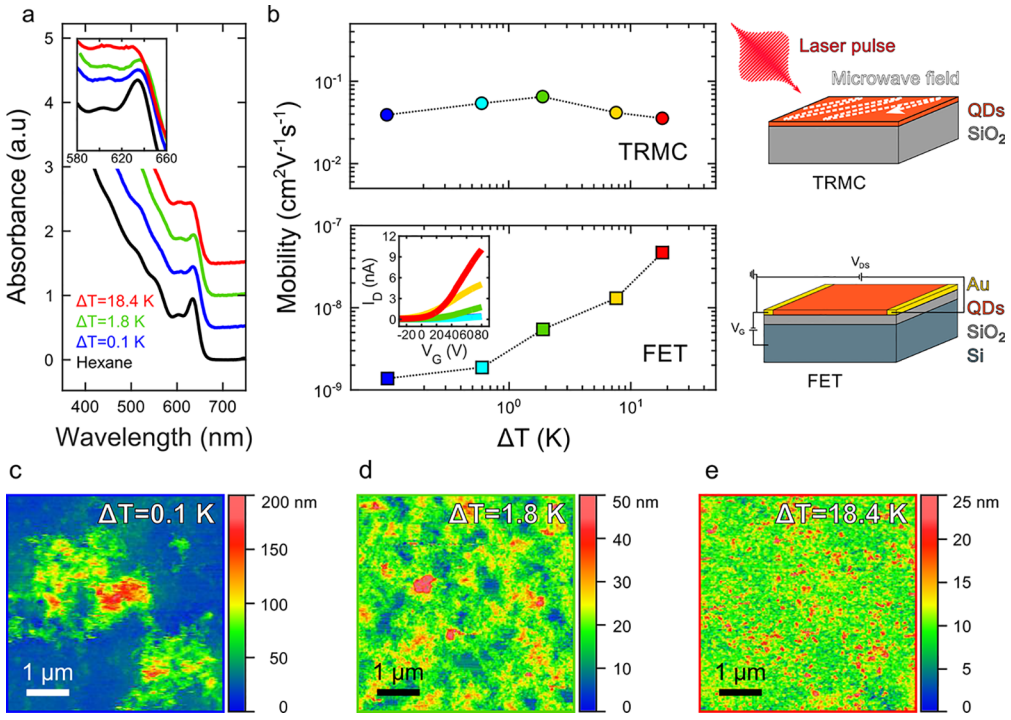

Figure 2. Optical and electronic transport properties of assembled QD superstructures. (a) Light absorption spectra of dispersed and assembled QDs. Black curve, bottom: QDs passivated by oleate ligands and dispersed in hexane; colored curves, top: QDs passivated by thiostannate ligands, assembled by critical Casimir forces and sedimented on a quartz substrate. Normalized curves have been shifted for clarity. Inset: Details of the first exciton peak for the various samples. (b) Electron mobility values measured with TRMC and FET devices, as a function of ΔT. Inset: Transfer curves of representative FET devices prepared at different temperatures, measured with 25 V channel bias. Right-hand side, top: Schematic of the TRMC measurement. The QD thin film is excited with a 630 nm nanosecond laser pulse inside a resonant microwave cavity. The generation of charge carriers causes a loss in microwave power reflected by the cavity, which is directly proportional to the mobility of charge carriers. Extrapolating the photoconductance of the sample for zero photon flux yields an estimate of the conductivity of the film.[35] Right-hand side, bottom: Schematic of an FET device. The QD thin film is deposited on a silicon oxide-covered n-doped silicon substrate. Charge transport is measured in the channel separated by two gold fingers, 2.5 μm apart, representing the drain and source electrodes, and using the silicon as the gate electrode. (c–e) AFM height maps of critical-Casimir-driven aggregates measured in the channel of the FET devices. Note the difference in height range shown in the color maps.

opalescence due to the onset of phase-separation was detected. The temperature was then decreased by ΔT, and the assembly vessel was submerged. The assembly vessel consisted of a 50 mL polypropylene centrifuge tube (Falcon) fitted with a conical polytetrafluoroethylene shape matching the inner dimensions of the tube to provide a flat bottom surface. A substrate (carbon-coated copper grid for electron microscopy, quartz for spectrophotometry and time-resolved microwave conductivity (TRMC), and patterned silicon for field-effect transistors (FETs)) was placed at the bottom of the vessel, and 5 mL of QD dispersion in the binary mixture was added. The water bath was held at a constant temperature for the whole duration of the assembly.

FET Characterization. Bottom gate/bottom contact field-effect transistors were fabricated on Si/SiO_2 wafers carrying ITO/Au electrodes (Fraunhofer) with a channel width of 10 mm and length of 2.5 μm. The wafers were cleaned by sonication in acetone (10 min) and isopropanol (10 min) before sample deposition. The electrical measurements were performed using a Keithley 4200SCS Semiconductor Characterization System in a nitrogen-filled glovebox. Prior to the measurement, the samples were briefly heated to 120 °C to remove any adsorbed water. The mobilities were extracted using the gradual channel approximation in the saturation regime.[30]

TRMC Characterization. A detailed description of this technique can be found elsewhere.[31] Briefly, the 1 mm-thick quartz substrate was placed in a microwave cavity driven at 8.5 GHz and illuminated at a wavelength of 630 nm using a 3 ns pulsed Nd:YAG laser at a 10 Hz repetition rate. The change in microwave power is measured and averaged over 1–10 min depending on the photon flux. The photon flux is reduced with a series of neutral density filters (increasing the averaging time with decreasing photon fluence) from 10^{15} to 10^{13} cm^{-2} to determine where higher order recombination processes no longer limit the signal. The mobility values reported here are given at a photon fluence where the mobility is independent of fluence ($\sim 10^{14}$ cm^{-2}).

Fractal Dimension Measurement. The two-dimensional fractal dimension was determined by using the box-counting method implemented as a Matlab script. Further details are available in the Supporting Information.

Pair Potential Modeling. QD pair potentials were determined as the superposition of van der Waals attraction, critical Casimir attraction, and screened electrostatics. Detailed procedures are described in the Supporting Information.

RESULTS AND DISCUSSION

Hydrophilic QDs dispersed in this binary mixture are expected to experience an increasingly attractive force upon approaching T_c (Figure 1b). Once the QD superstructures have sufficiently

DOI: 10.1021/acs.jpcc.9b02033
J. Phys. Chem. C 2019, 123, 13451–13457

grown, the assemblies sediment and deposit on a substrate placed at the bottom of the vessel. The deposits retrieved after different growth times show indeed growing superstructures (Figure S1), contrary to the dots dispersed in water alone, which are stable and do not aggregate. In the binary solvent, already after a few minutes at ΔT = 7.8 K, QD aggregates are visible on the transmission electron microscope (TEM) grid, ranging from tens to hundreds of nanometers in size.

We observe a clear dependence of the aggregate morphology on the temperature of the solvent as shown in Figure 1c−e, displaying superstructures grown at ΔT = 0.1, 1.8, and 18.4 K for 84 h. While temperatures closer to T_c induce the growth of larger, branched structures (Figure 1c), temperatures further away induce the growth of smaller, globular structures (Figure 1e). This suggests that the stronger critical Casimir attraction closer to T_c causes a more ramified morphology, whereas the weaker attraction further away from T_c allows particles to rearrange into more compact structures.

This morphological control allows us to elucidate the effect of morphology on the optical properties of the assembled QD structures. After growing and depositing QD superstructures on a quartz substrate, we measure their light absorption spectra as shown in Figure 2a. As a reference, we also show the spectrum of QDs dispersed in hexane stabilized by long, insulating oleate ligands. While the overall spectral shape and excitonic peak positions are unchanged for samples grown at different ΔT, demonstrating that the QD size is unaffected in agreement with X-ray scattering results (Figure S2a,b),[29] the first exciton peak loses its distinction as the half-width at half-maximum increases from 14 to 19 nm, or from 27 to 35 meV in energy units (see inset). This broadening is particularly evident at wavelengths around 620 nm, where the first and second exciton peaks start merging and the prominence of the third peak almost vanishes. The effect becomes increasingly pronounced with increasing ΔT, corresponding to weaker Casimir attraction. The peak broadening is likely due to electronic coupling between neighboring QDs, as opposed to the case of dispersed QDs, suggesting the overlap of single QD electronic wave functions in the dense, rearranged QD aggregates promoted by the short thiostannate ligands.[32,33]

To investigate in more detail the interdot electronic coupling and its dependence on the growth temperature, we measure the electronic transport properties of the QD aggregates deposited on a substrate. The charge carrier mobility represents the figure of merit in this regard, providing further insight into the extent of electronic coupling (Figure 2b).[34,35] We first investigate electronic coupling on a local scale by using time-resolved microwave conductivity (TRMC),[31] a contact-less spectroscopic technique probing charge carrier transport on a scale of $\delta_{TRMC} \approx 28$ nm for CdSe (Figures 2b and S3).[25] We find mobility values of 4 to 7 × 10^{-2} cm^2 V^{-1} s^{-1}, in good agreement with values reported in the literature for CdSe QDs passivated with thiostannate ligands,[8] and rather independent of the strength of the attractive potential used to drive the assembly (Figure 2b). Charge transport on the length scale of a few QDs, as it is measured using TRMC, is thus unaffected by the superstructure morphology. We then probe the electronic transport on a larger scale (micrometers) by employing Casimir-driven QD thin-films in field-effect transistors (FETs, Figure 2b inset) with a channel length of δ_{FET} = 2.5 μm. We find that the films behave as n-type semiconductors, consistent with CdSe QDs passivated by inorganic ligands,[8] with the onset voltage being unaffected by ΔT, indicating that the different deposition conditions do not influence the concentration of dopants (Figure S4). Remarkably, the electron mobility rises strongly with ΔT, suggesting that the global charge transport is strongly affected by the morphological changes, in line with the gradual broadening of the absorption peak in Figure 2a. At the same time, these mobility values are orders of magnitude lower than those found with TRMC, demonstrating the much longer length scales probed with the transistor measurements, and the presence of electronic traps in the film (Figure S4).

TRMC and FETs provide complementary information concerning the electronic transport in QD films. The TMRC mobility probed on a mean path of $\delta_{TRMC}/\sigma_{QD} \approx 4$ QDs provides a good indication of the local tunneling rate between neighboring dots, averaged over the film.[35] Instead, the FET mobility probes a much longer length scale $\delta_{FET} \gg \delta_{TRMC}$ that is mainly determined by the path of lowest resistance in the disordered QD solid, represented by domains of highly coupled QDs.[7] The constant TMRC mobility with respect to ΔT is in line with the constant excitonic peak position, suggesting unchanged average confinement and interdot interaction. On the other hand, the increase of FET mobility with ΔT is consistent with the broadening of the excitonic peaks, which reveals the onset of electronic energetic disorder due to certain regions exhibiting stronger coupling with respect to the rest of the film, thus giving rise to percolative transport.

In situ atomic force microscopy can investigate the origin of this conductivity increase by directly probing the QD film morphology in the FET channel (Figure 2c−e). We find a substantial decrease in film thickness and roughness with increasing ΔT, supporting the view that weakly attractive QDs at high ΔT form more compact superstructures. These may even deform upon deposition on the substrate, yielding a more two-dimensional film morphology that likely explains the gradual increase of in-plane conductivity with ΔT. While this superstructure morphology only weakly affects the charge carrier mobility values measured by TRMC on a mean path of $\delta_{TRMC}/\sigma_{QD} \approx 4$ QDs, the charge transport probed by FET over longer distances of $\delta_{FET}/\sigma_{QD} \approx 400$ QD diameters reflects the increase in the number of parallel percolative paths available in the plane of conduction.

These percolative paths result from the space-spanning properties of the aggregate. To study this in more detail, we employ the box-counting method to investigate the scaling of the cluster mass as a function of length,[36] see Figure 3a. We find a power-law relation over the available 3 orders of magnitude in length scale, indicating the lack of a dominant length scale of the system and therefore a fractal structure.[36] Fractals are characterized by the so-called fractal dimension d_f, describing their space-filling properties; in two dimensions, d_f varies between d_f = 1 and d_f = 2 to indicate, respectively, linear and space-filling planar structures. As an example, the measured fractal dimension of the aggregate shown in Figure 3a is d_f = 1.73, consistent with the values found for structures grown by diffusion-limited aggregation with a low sticking probability (Figure S5). A low sticking probability implies that the growing aggregate will explore a large number of configurations tending to equilibrium structures, characterized by a high fractal dimension.[37]

Measuring hundreds of superstructures for each ΔT value, we build the histograms shown in Figure 3b, whose maximum is at around $d_f \sim 1.5$, corresponding to a high sticking probability of ~1 (Figure S5). Since the magnitude of the

DOI: 10.1021/acs.jpcc.9b02033
J. Phys. Chem. C 2019, 123, 13451−13457

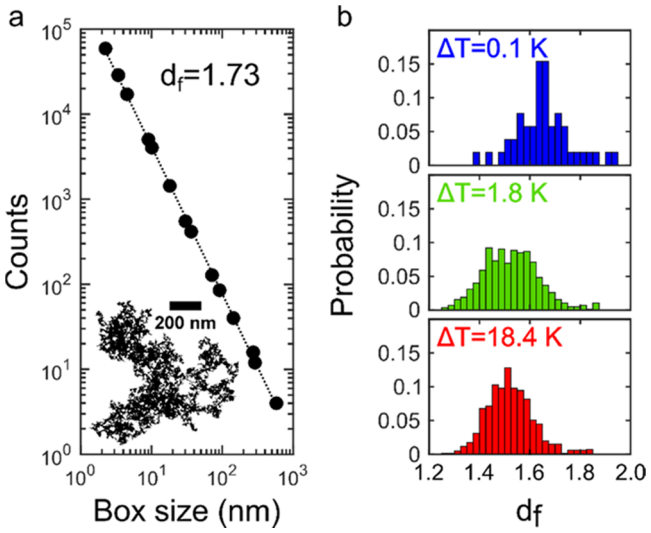

Figure 3. Microstructure and fractal dimension of QD superstructures. (a) Box-counting method applied to a QD superstructure grown at ΔT = 7.8 K. The box count decreases with box size, following a power-law relation with exponent d_f = 1.73, the fractal dimension. Inset: QD superstructure used for the box-counting. (b) Two-dimensional fractal dimension histograms extracted by analyzing several hundred fractal aggregates for each ΔT value.

Casimir interaction varies with ΔT, we expect a dependence of d_f on ΔT.[38] Contrary to expectations, however, the distribution of these two-dimensional fractal dimensions is fairly robust upon varying ΔT. A comparison of the superstructures reveals that while the branched structures grown at lower ΔT seem unaffected by deposition on the substrates, the globular structures grown at higher ΔT appear to deform upon sedimentation, yielding three-dimensional, thick cores surrounded by quasi two-dimensional shells (Figure 1c–e). We attribute this to the softness of structures grown at higher ΔT, deforming upon contact with the substrate. These morphological differences ultimately are at the origin of the optical and transport properties shown in Figure 2.

To rationalize these findings, we propose a simple pair potential model. The observation of stable superstructures after solvent removal suggests that eventually van der Waals forces bind the particles irreversibly. On the other hand, the temperature-dependent morphology of the aggregates and their deformation upon sedimentation indicate that weaker critical Casimir forces drive their initial growth. We hence hypothesize that critical Casimir forces control the initial reversible assembly, whereas van der Waals forces lead to their immobilization at later stages and during drying.[39] To elucidate the transition from reversible Casimir to irreversible van der Waals interactions, we model the pair potential by superimposing the temperature-dependent critical Casimir interaction onto standard DLVO interactions, describing the balance of electrostatic repulsion and van der Waals attraction. The former is determined via explicit critical Casimir modeling using the correlation lengths and particle sizes determined by X-ray scattering and TEM (Figure S2d),[16] whereas the electrostatic interaction is corrected tentatively for ion-solvent fluctuation coupling.[40] The details are provided in the Supporting Information file. The full modeling of critical Casimir interactions, in particular for nanoparticles where many-body effects are likely to become important, is a current analytical challenge and beyond the scope of this work. Therefore, here we rely on a simplified treatment of the pair potential based on the Derjaguin approximation. This approximation does not strictly hold for the lowest ΔT investigated here, yet, the resulting potential qualitatively agrees with our observations: As T_c is approached, the critical Casimir potential deepens, leading to a well-defined secondary minimum, as shown in Figure 4. Consistent with this simple

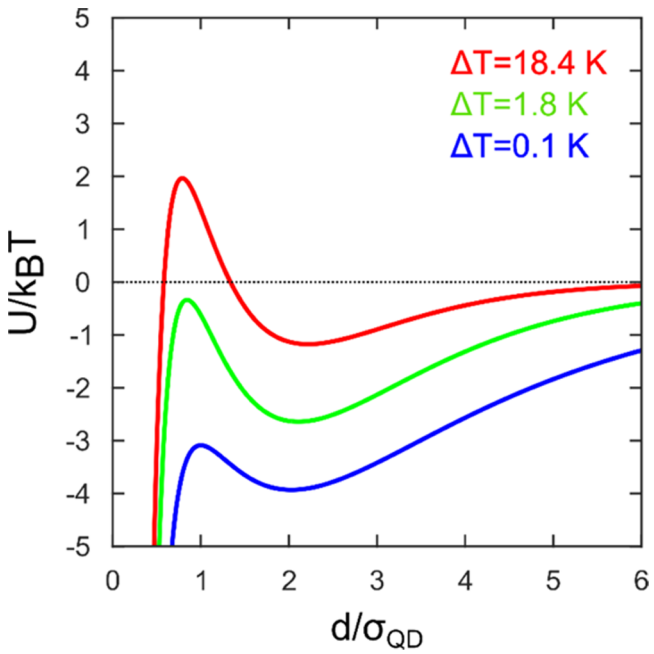

Figure 4. QD pair-potential. Pair-potentials of σ_{QD} = 6.5 nm CdSe QDs in the binary solvent, modeled from superimposed critical Casimir, van der Waals, and electrostatic interactions, for three different ΔT values.

model, we observe that at large ΔT, QDs are weakly attractive but stable against the primary van der Waals minimum due to a relatively high energy barrier separating the primary and secondary minima. This scenario gradually evolves at temperatures closer to T_c: QDs become more attractive as the critical Casimir force increases, and the barrier height decreases, making irreversible aggregation more likely. This transition from weakly- to strongly-attractive QDs qualitatively reflects our experimental observations: at larger ΔT, some reversibility of the aggregation is observed, whereas at small ΔT, this reversibility is lost and the structures become permanently aggregated. This reversibility qualitatively explains the experimentally observed marked morphological differences between superstructures grown at different ΔT. The critical Casimir force thus allows reversible assembly control, even annealing of QD structures at large ΔT, and fixing these structures at small ΔT. This temperature control is at the origin of the temperature-dependent optical and transport properties shown in Figure 2. These results open up new opportunities for the purposeful assembly of QDs based on the temperature control of nanoparticle interactions in near-critical binary solvents.

CONCLUSIONS

We have shown that critical Casimir forces between nanoparticles provide a powerful tool to tailor the morphology of QD superstructures. By mildly adjusting the temperature of the

DOI: 10.1021/acs.jpcc.9b02033
J. Phys. Chem. C 2019, 123, 13451−13457

solution, we drive the assembly of QDs into superstructures that grow in time to reach sizes compatible with device application. Temperature controls the superstructure morphology: While higher temperatures (lower ΔT) induce the growth of branched structures, lower temperatures (higher ΔT) allow for softer and denser aggregates. Upon deposition on the substrate, these soft aggregates deform, increasing the surface coverage and leading to enhanced electronic coupling. In turn, this results in more percolative pathways for conduction, allowing for higher charge carrier mobility. The choice of substrate can span virtually any solid-state substrate, allowing a full topographic, optical, and electronic characterization of the critical Casimir-grown QD superstructures. Unlike previous applications of critical Casimir forces used to model reversible colloidal phase transitions and aggregation, we here explore a new realm of applications to produce permanently assembled nanostructures for devices. The permanent aggregation crucial for these applications is possible due to the ultimate prevalence of van der Waals forces at the nanoscale, whereas the initial structure formation is set by critical Casimir interactions, allowing fine temperature control of the structural morphology. We anticipate that by controlling not only the particles' interactions but also their interaction with the substrate, critical Casimir forces should be able to promote the controlled deposition of QDs on a substrate, thereby driving two-dimensional growth or QD epitaxy.[42,43] Finally, the novel application of critical Casimir forces to nanoscale building blocks extends previous critical Casimir research to a reversed length scale regime, where the particles become of the order of or even smaller than the solvent fluctuations, promoting many-body effects and calling for new theoretical models of particle interactions.[41]

■ ASSOCIATED CONTENT

Supporting Information

The Supporting Information is available free of charge on the ACS Publications website at DOI: 10.1021/acs.jpcc.9b02033.

Details concerning CdSe QD synthesis, thiostannate ligand synthesis, ligand exchange procedures, critical Casimir assembly, and experimental and modeling techniques used in this work (PDF)

■ AUTHOR INFORMATION

Corresponding Author

*E-mail: p.schall@uva.nl.

ORCID

Emanuele Marino: 0000-0002-0793-9796

Daniel M. Balazs: 0000-0001-7597-043X

Ryan W. Crisp: 0000-0002-3703-9617

Maria A. Loi: 0000-0002-7985-7431

Present Addresses

[#]Department of Chemistry, University of Pennsylvania, Philadelphia, Pennsylvania 19104, United States (E.M.).

[▽]Department of Chemical and Biomolecular Engineering, Cornell University, Ithaca, New York 14853, United States (D.M.B.).

Author Contributions

E.M., T.E.K., and P.S. conceived the project. E.M. synthesized QDs and ligands. E.M. and T.E.K. assembled QDs via critical Casimir forces. E.M., T.E.K., D.H.-M., and P.S. measured SAXS patterns. D.M.B. measured and analyzed FET devices. R.W.C. measured and analyzed TRMC transients. All authors contributed to the interpretation of experimental results. E.M. modeled diffusion-limited aggregation with variable sticking coefficients and QD pair potentials. The manuscript was written through contributions of all authors. All authors have given approval to the final version of the manuscript.

Notes

The authors declare no competing financial interest.

■ ACKNOWLEDGMENTS

M.A.L. and D.M.B. are grateful to the European Research Council for funding under the ERC Starting Grant No. 306983 "HySPOD". R.W.C. was supported by STW (project no. 13903, Stable and Non-Toxic Nanocrystal Solar Cells). T.E.K. and P.S. acknowledge, respectively, Veni and Vici grants from the Netherlands Organisation for Scientific Research (NWO). Beamtime at BM26B "DUBBLE" beamline, ESRF, was supported by NWO (experiment no. 26-02-740). E.M., T.E.K., and P.S. thank the staff at DUBBLE for technical support during the beamtime. E.M. and P.S. are grateful to Svyatoslav Kondrat for helpful discussions.

■ REFERENCES

(1) Ganesan, A.; Houtepen, A.; Crisp, R. Quantum Dot Solar Cells: Small Beginnings Have Large Impacts. *Appl. Sci.* **2018**, *8*, No. 1867.

(2) Boles, M. A.; Engel, M.; Talapin, D. V. Self-assembly of Colloidal Nanocrystals: From Intricate Structures to Functional Materials. *Chem. Rev.* **2016**, *116*, 11220−11289.

(3) Kagan, C. R.; Lifshitz, E.; Sargent, E. H.; Talapin, D. V. Building Devices from Colloidal Quantum Dots. *Science* **2016**, *353*, No. aac5523.

(4) Scher, H.; Zallen, R. Critical Density in Percolation Processes. *J. Chem. Phys.* **1970**, *53*, 3759−3761.

(5) Efros, A.; Shklovskii, B. Critical Behaviour of Conductivity and Dielectric Constant Near the Metal-non-metal Transition Threshold. *Phys. Status Solidi B* **1976**, *76*, 475−485.

(6) Kagan, C. R.; Murray, C. B. Charge Transport in Strongly Coupled Quantum Dot Solids. *Nat. Nanotechnol.* **2015**, *10*, No. 1013.

(7) Balazs, D. M.; Matysiak, B. M.; Momand, J.; Shulga, A. G.; Ibáñez, M.; Kovalenko, M. V.; Kooi, B. J.; Loi, M. A. Electron Mobility of 24 cm^2 V^{-1} s^{-1} in PbSe Colloidal-quantum-dot Superlattices. *Adv. Mater.* **2018**, *30*, No. 1802265.

(8) Kovalenko, M. V.; Scheele, M.; Talapin, D. V. Colloidal Nanocrystals with Molecular Metal Chalcogenide Surface Ligands. *Science* **2009**, *324*, 1417−1420.

(9) André, A.; Weber, M.; Wurst, K. M.; Maiti, S.; Schreiber, F.; Scheele, M. Electron-conducting PbS Nanocrystal Superlattices with Long-range Order Enabled by Terthiophene Molecular Linkers. *ACS Appl. Mater. Interfaces* **2018**, *10*, 24708−24714.

(10) Balazs, D. M.; Loi, M. A. Lead-chalcogenide Colloidal-quantum-dot Solids: Novel Assembly Methods, Electronic Structure Control, and Application Prospects. *Adv. Mater.* **2018**, *30*, No. 1800082.

(11) Gilmore, R. H.; Winslow, S. W.; Lee, E. M. Y.; Ashner, M. N.; Yager, K. G.; Willard, A. P.; Tisdale, W. A. Inverse Temperature Dependence of Charge Carrier Hopping in Quantum Dot Solids. *ACS Nano* **2018**, No. 7741.

(12) Baranov, D.; Fiore, A.; van Huis, M.; Giannini, C.; Falqui, A.; Lafont, U.; Zandbergen, H.; Zanella, M.; Cingolani, R.; Manna, L. Assembly of Colloidal Semiconductor Nanorods in Solution by Depletion Attraction. *Nano Lett.* **2010**, *10*, 743−749.

(13) Erb, R. M.; Son, H. S.; Samanta, B.; Rotello, V. M.; Yellen, B. B. Magnetic Assembly of Colloidal Superstructures with Multipole Symmetry. *Nature* **2009**, *457*, No. 999.

DOI: 10.1021/acs.jpcc.9b02033
J. Phys. Chem. C 2019, 123, 13451−13457

(14) Nykypanchuk, D.; Maye, M. M.; van der Lelie, D.; Gang, O. DNA-guided Crystallization of Colloidal Nanoparticles. *Nature* **2008**, *451*, No. 549.
(15) Beysens, D.; Estève, D. Adsorption Phenomena at the Surface of Silica Spheres in a Binary Liquid Mixture. *Phys. Rev. Lett.* **1985**, *54*, 2123−2126.
(16) Bonn, D.; Otwinowski, J.; Sacanna, S.; Guo, H.; Wegdam, G.; Schall, P. Direct Observation of Colloidal Aggregation by Critical Casimir Forces. *Phys. Rev. Lett.* **2009**, *103*, No. 156101.
(17) Veen, S. J.; Antoniuk, O.; Weber, B.; Potenza, M. A. C.; Mazzoni, S.; Schall, P.; Wegdam, G. H. Colloidal Aggregation in Microgravity by Critical Casimir Forces. *Phys. Rev. Lett.* **2012**, *109*, No. 248302.
(18) Zvyagolskaya, O.; Archer, A. J.; Bechinger, C. Criticality and Phase Separation in a Two-dimensional Binary Colloidal Fluid Induced by the Solvent Critical Behavior. *Europhys. Lett.* **2011**, *96*, No. 28005.
(19) Hertlein, C.; Helden, L.; Gambassi, A.; Dietrich, S.; Bechinger, C. Direct Measurement of Critical Casimir Forces. *Nature* **2008**, *451*, No. 172.
(20) Maciołek, A.; Dietrich, S. Collective Behavior of Colloids due to Critical Casimir Interactions. *Rev. Mod. Phys.* **2018**, *90*, No. 045001.
(21) Marino, E.; Kodger, T. E.; ten Hove, J. B.; Velders, A. H.; Schall, P. Assembling Quantum Dots via Critical Casimir Forces. *Sol. Energy Mater. Sol. Cells* **2016**, *158*, 154−159.
(22) Carion, O.; Mahler, B.; Pons, T.; Dubertret, B. Synthesis, Encapsulation, Purification and Coupling of Single Quantum Dots in Phospholipid Micelles for Their Use in Cellular and In Vivo Imaging. *Nat. Protoc.* **2007**, *2*, No. 2383.
(23) Chernomordik, B. D.; Marshall, A. R.; Pach, G. F.; Luther, J. M.; Beard, M. C. Quantum Dot Solar Cell Fabrication Protocols. *Chem. Mater.* **2016**, *29*, 189−198.
(24) Kovalenko, M. V.; Bodnarchuk, M. I.; Zaumseil, J.; Lee, J.-S.; Talapin, D. V. Expanding the Chemical Versatility of Colloidal Nanocrystals Capped with Molecular Metal Chalcogenide Ligands. *J. Am. Chem. Soc.* **2010**, *132*, 10085−10092.
(25) Marino, E.; Kodger, T. E.; Crisp, R. W.; Timmerman, D.; MacArthur, K. E.; Heggen, M.; Schall, P. Repairing Nanoparticle Surface Defects. *Angew. Chem.* **2017**, *129*, 13983−13987.
(26) Fisher, M.; de Gennes, P. Phenomena at the Walls in a Critical Binary Mixture. *CR Seances Acad. Sci., Ser. B* **1978**, *287*, No. 207.
(27) Stuij, S.; Labbé-Laurent, M.; Kodger, T.; Maciołek, A.; Schall, P. Critical Casimir Interactions Between Colloids Around the Critical Point of Binary Solvents. *Soft Matter* **2017**, *13*, 5233−5249.
(28) Krech, M. Fluctuation-induced Forces in Critical Fluids. *J. Phys.: Condens. Matter* **1999**, *11*, No. R391.
(29) Yu, W. W.; Qu, L.; Guo, W.; Peng, X. Experimental Determination of the Extinction Coefficient of CdTe, CdSe, and CdS Nanocrystals. *Chem. Mater.* **2003**, *15*, 2854−2860.
(30) Sze, S. M.; Ng, K. K. In *Physics of Semiconductor Devices*; John Wiley & Sons, 2006.
(31) Schins, J. M.; Talgorn, E. Conductive Response of a Photo-excited Sample in a Radio-frequent Driven Resonance Cavity. *Rev. Sci. Instrum.* **2011**, *82*, No. 064703.
(32) Crisp, R. W.; Schrauben, J. N.; Beard, M. C.; Luther, J. M.; Johnson, J. C. Coherent Exciton Delocalization in Strongly Coupled Quantum Dot Arrays. *Nano Lett.* **2013**, *13*, 4862−4869.
(33) Koole, R.; Liljeroth, P.; de Mello Donegá, C.; Vanmaekelbergh, D.; Meijerink, A. Electronic Coupling and Exciton Energy Transfer in CdTe Quantum-dot Molecules. *J. Am. Chem. Soc.* **2006**, *128*, 10436−10441.
(34) Crisp, R. W.; Kirkwood, N.; Grimaldi, G.; Kinge, S.; Siebbeles, L. D.; Houtepen, A. J. Highly-photoconductive InP Quantum Dots Films and Solar Cells. *ACS Appl. Energy Mater.* **2018**, No. 1453.
(35) Crisp, R. W.; Callahan, R.; Reid, O. G.; Dolzhnikov, D. S.; Talapin, D. V.; Rumbles, G.; Luther, J. M.; Kopidakis, N. Photoconductivity of CdTe Nanocrystal-Based Thin Films: $Te2^{-}$ Ligands Lead To Charge Carrier Diffusion Lengths Over 2 μm. *J. Phys. Chem. Lett.* **2015**, *6*, 4815−4821.
(36) Mandelbrot, B. B. In *The Fractal Geometry of Nature*; WH Freeman: NY, 1983; Vol. *173*.
(37) Weitz, D.; Huang, J.; Lin, M.; Sung, J. Limits of the Fractal Dimension for Irreversible Kinetic Aggregation of Gold Colloids. *Phys. Rev. Lett.* **1985**, *54*, No. 1416.
(38) Shelke, P. B.; Nguyen, V.; Limaye, A.; Schall, P. Controlling Colloidal Morphologies by Critical Casimir Forces. *Adv. Mater.* **2013**, *25*, 1499−1503.
(39) Marino, E.; Kodger, T. E.; Wegdam, G. H.; Schall, P. Revealing Driving Forces in Quantum Dot Supercrystal Assembly. *Adv. Mater.* **2018**, *30*, No. 1803433.
(40) Nguyen, V.; Dang, M.; Nguyen, T.; Schall, P. Critical Casimir Forces for Colloidal Assembly. *J. Phys.: Condens. Matter* **2016**, *28*, No. 043001.
(41) Paladugu, S.; Callegari, A.; Tuna, Y.; Barth, L.; Dietrich, S.; Gambassi, A.; Volpe, G. Nonadditivity of Critical Casimir Forces. *Nat. Commun.* **2016**, *7*, No. 11403.
(42) Rupich, S. M.; Castro, F. C.; Irvine, W. T.; Talapin, D. V. Soft Epitaxy of Nanocrystal Superlattices. *Nat. Commun.* **2014**, *5*, No. 5045.
(43) Wang, M. X.; Seo, S. E.; Gabrys, P. A.; Fleischman, D.; Lee, B.; Kim, Y.; Atwater, H. A.; Macfarlane, R. J.; Mirkin, C. A. Epitaxy: Programmable Atom Equivalents Versus Atoms. *ACS Nano* **2016**, *11*, 180−185.

DOI: 10.1021/acs.jpcc.9b02033
J. Phys. Chem. C 2019, 123, 13451−13457